AO4ELT7 - June 2023 - Avignon

Revisiting Shack-Hartmann wavefront sensor design for space-ground communications in strong scintillation conditions

Timothée Vène[a], Aurélie Montmerle Bonnefois[a], Jean-Marc Conan[a], Laurie Paillier[a], and Laurent M. Mugnier[a]

[a]ONERA, DOTA, Université Paris Saclay, F-92322 Châtillon, France

ABSTRACT

The increasing need for high throughput and security in ground-satellite links is fostering the development of optical telecommunication solutions to compensate for the atmospheric turbulence by adaptive optics (AO). In the case of a Low-Earth Orbit (LEO) satellite, it is crucial to maximize the duration of the downlink, even at low elevations, since a satellite spends half of the time it is viewable by a ground station between 30° and 10° elevations. However, as the elevation decreases, the path of the beam through the atmosphere gets longer, and the perturbations in the pupil of the receiver terminal get stronger. This is all the more noticeable as we go from a weak perturbation regime to a strong perturbation regime. This is a critical issue for AO systems since an inhomogeneous distribution of intensity leads to a reduced performance of the wavefront sensor (WFS) and thus hinders the correction. Regarding the Shack-Hartmann wavefront sensor (SHWFS), scintillation induces a wide signal range between the various subapertures causing part of them to be saturated and others to be extinguished. Besides, some subapertures spots suffer from strong diffraction effects induced by non-uniform intensity distribution, making it difficult to obtain accurate centroid measurements. We propose here to study the effect of the number of subapertures of a SHWFS on its performance in the presence of amplitude perturbations representative of a LEO to ground link. We show preliminary results –while neglecting noise and dynamic range limitations– leading to the conclusion that increasing the SHWFS sampling of the pupil plane improves its robustness to scintillation.

Keywords: optical communication, adaptive optics, wavefront sensing, Shack-Hartmann, strong perturbations, scintillation

1. INTRODUCTION

In the case of Low Earth Orbit (LEO) satellites, there is a need for high-speed downlinks, to transfer of Earth observation images for instance. To increase this throughput, optical solutions are increasingly being considered. Besides, the directivity of the laser beam ensures a better security compared to RF links. Nevertheless, atmospheric turbulence represents a major problem for optical communication. Indeed, because of the turbulence along the

---

Further author information: (Send correspondence to Timothée VENE)
Timothée VENE: E-mail: timothee.vene@onera.fr

line of sight, the beam wavefront is distorted during propagation and this can lead to significant variations in the received signal and even interruptions due to fadings. Hence the use of adaptive optics (AO) to compensate for this deformation and obtain a sufficiently high level of received signal coupled in a Single Mode Fiber (SMF) in the ground station terminal. However, the state-of-the-art AO is designed to work in a certain turbulence regime: the weak perturbation one which corresponds to the case of high elevations for a LEO satellite (between 90° and 30°). But at lower elevations, the part of the link taking place within the atmosphere becomes longer: not only do the phase deformations get more severe but also amplitude fluctuations (i.e scintillation) become stronger ($\sigma_\chi^2 > 0.3$). This is the strong perturbation regime where the performance of the AO system is not guaranteed. Nonetheless, these low elevations are crucial because LEO satellites spend half of the time they are in visibility of a given station between 30° and 10°.

Scintillation affects an AO system by preventing the wavefront sensor (WFS) from correctly measuring the phase deformation inducing a biased correction of the wavefront by the deformable mirror. In the pupil plane of the WFS, these large intensity fluctuations imply branch points (i.e points where the intensity cancels) responsible for the decrease of the WFS efficiency as pointed out by Barchers [1] and Primmerman[9]. But these branch points are less of a problem regarding optical communication applications where the aim is to couple as much flux as possible in a SMF: the correction at points without intensity is therefore not an issue. In order to mitigate the effect of scintillation, alternative WFSs are developed. For example, there are solutions based on self-referenced interferometry featuring a large dynamic range [10], [7], and also some solutions using variations of the Shack-Hartmann WFS (SHWFS) as presented in Lechner et al.(2020) [4]. However, at the moment, there is no theoretical study on wavefront sensing in the presence of scintillation describing the optimal WFS to use in this case.

In this communication, we illustrate the particularity of wavefront sensing with scintillation by studying the SHWFS, a well spread WFS featuring linear behaviour and a wide sensing range while being simple to model. Scintillation can cause a non-uniform distribution of intensity at a subaperture scale, and Mahé et al.(2000) [5] have shown that it induces a bias on the slope measurement performed by a SHWFS. Our goal here is to study the effect of the number of subapertures on the performance of the SHWFS in order to optimize its design.

This paper presents preliminary results of this study. We are neglecting at first the noise during the measurement and the limitations due to the dynamic range of the sensor, thus focusing solely on the effect of intensity inhomogeneities on the SHWFS measurements.
In section 2, we present the analytical background of the wavefront analysis with a SHWFS and the special features due to the presence of scintillation. In Section 3, we describe the chosen atmospheric turbulence scenarios, representative of a LEO-to-ground link featuring strong perturbations. In Section 4, we explain the modeling of the measurement by three SHWFS designs and we propose a new metric robust to branch points as well as representative of the ability of the AO system to couple flux efficiently in a SMF. Finally, in Section 5, we present some preliminary results showing the improvement brought by smaller subapertures regarding robustness to scintillation, and we discuss the effect of intensity distribution in the subapertures on the measurement error due to scintillation.

2. SHWFS IN THE PRESENCE OF SCINTILLATION

As mentioned in the previous Section, we choose the SHWFS to illustrate wavefront sensing in the presence of scintillation. Its working principle is illustrated in Fig. 1 in both weak and strong perturbation regimes. The incoming field, expressed as $\psi(x,y,t) = A(x,y,t)e^{i\varphi(x,y,t)}$ (where $A(x,y,t) = e^{\chi(x,y,t)}$), is sampled by a microlens array and then focused by each subaperture into Point-spread Functions (PSF) at the focal plane: the displacement of these PSF is related to the phase deformation seen by each subaperture.

Assuming infinite field of view, continuous support and no noise, we have the following relation between the displacement of the spot and the phase gradient[5]:

$$\Delta x \propto \frac{\iint_S I(x,y)\frac{\partial\varphi(x,y)}{\partial x}\mathrm{d}x\mathrm{d}y}{\iint_S I(x,y)\mathrm{d}x\mathrm{d}y} \tag{1}$$

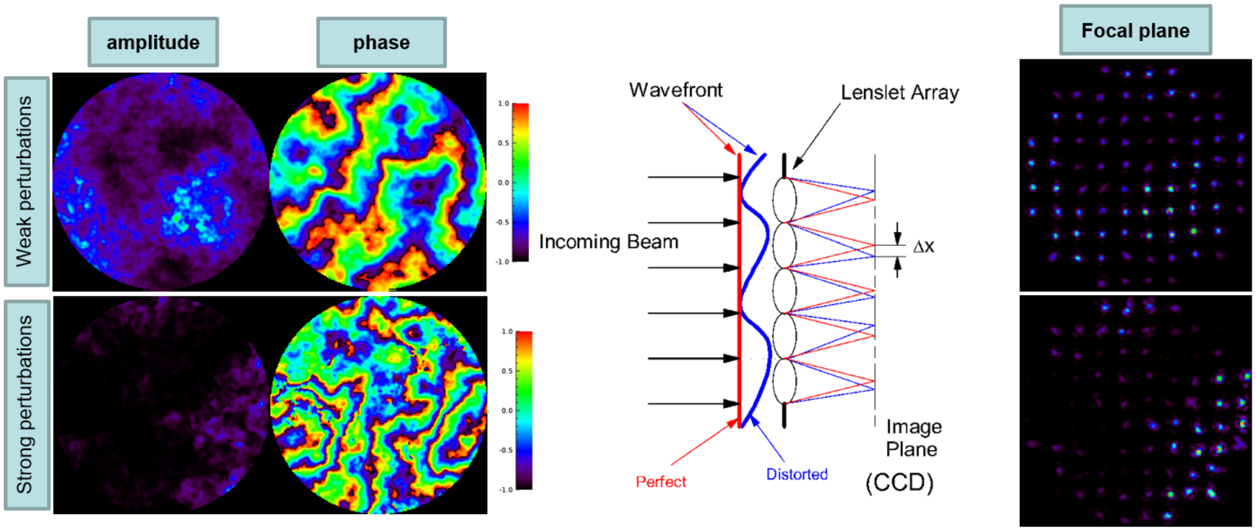

Figure 1: Effect of scintillation on the SHWFS. (Upper row) Weak perturbation case: the spots at the focal plane enable to measure the wavefront. (Bottom row) Strong perturbations case: the amplitude perturbation is more severe, resulting in some spots being extinguished, some being saturated and some suffering non-uniform intensity distribution.

where, Δx is the displacement of the spot along the x axis, S is the support, φ and I are respectively the phase and the intensity of the incoming complex field. It corresponds to the weighing of the phase gradient by the intensity distribution.

However, the reconstruction model assumes that the intensity in the subapertures is uniform. It is therefore based on the following model:

$$\Delta x \propto \iint_S \frac{\partial \varphi(x,y)}{\partial x} \mathrm{d}x\mathrm{d}y \tag{2}$$

This assumption is valid in the weak perturbation regime. But, considering strong perturbations and scintillation, the non-uniformity of the intensity distribution in the subapertures causes biases in the SHWFS measurements and reconstruction. The latter results from the difference between Eqs. 1 and 2 and has been pointed out by Mahé et al.(2000) [5].

3. CHOICE AND SIMULATION OF TURBULENCE SCENARIOS REPRESENTATIVE OF A LEO-TO-GROUND LINK

For this study, we need to simulate complex fields that are representative of a LEO-to-ground link at low elevation, hence presenting scintillation. To do so, we want turbulence profiles corresponding to daytime strong perturbations in suburban areas for satellite elevation between 30° and 10°. In practice, we use the MOSPAR turbulence profiles database[13], generated by combining high altitude profiles from Paranal [8] and ground level measurements through Monin-Obhukov similitude law.

From these profiles, we compute the integrated parameter σ_χ^2, or the log-amplitude variance, with the following formula in Rytov regime:

$$\sigma^2_{\chi Rytov} = 0,5631(\frac{2\pi}{\lambda})^{7/6} \int_0^{z_{max}} z^{5/6} C_n^2(z)\mathrm{d}z \tag{3}$$

where λ is the wavelength (1.55µm here), and C_n^2 the turbulence strength. The log-amplitude variance is an indicator of the scintillation strength in a given profile. From experimental data (Gracheva 1966 [3]), the strong perturbation regime is considered to be reached when the Rytov variance exceeds 0.3. In this paper, we focus on the MOSPAR9090, MOSPAR9797, and MOSPAR9999, three strongly turbulent profiles at elevations from 30° to 10°. The "9X9X" terminology is related to the distribution of r_0 and θ_0 in the database. For instance with the

MOSPAR9090, it means that this turbulence profile is more severe than 90% of the database, regarding both Fried parameter and anisoplanetism angle. The integrated parameters of these profiles at the elevation of interest are presented in Tab. 1. They have been computed using Rytov approximation based analytical models. These profiles give access to both weak and strong perturbation regimes.

	profile 90				**profile 97**				**profile 99**			
	30°	**20°**	**15°**	**10°**	**30°**	**20°**	**15°**	**10°**	**30°**	**20°**	**15°**	**10°**
r_0 (cm)	4,027	3,207	2,714	2,137	3,18	2,533	2,143	1,688	2,626	2,092	1,77	1,394
D/r_0 (D=50cm)	12,42	15,59	18,42	23,40	15,72	19,74	23,33	29,62	19,04	23,90	28,25	35,87
$\sigma^2_{\chi Rytov}(rad^2)$	0,0786	0,1573	0,26	0,5264	0,1089	0,218	0,3606	0,7303	0,1327	0,2658	0,4396	0,8891
θ_0 (µrad)	6,83	3,75	2,43	1,32	5,62	3,08	2,00	1,10	4,81	2,64	1,72	0,94

Table 1: Integrated parameters of the studied profiles.

From these profiles, we simulate the propagation of the beam through atmospheric turbulence using the split-step algorithm PILOT developed by ONERA. It models turbulence effects by using Fresnel propagation through multiple phase screens. It is able to simulate propagation through the atmosphere both in weak and strong perturbation regimes.

4. MEASUREMENT MODEL AND PERFORMANCE METRIC

The SHWFS can be regarded as a field sensor rather than only a wavefront sensor. Indeed, as explained in Section 2, intensity plays an essential role in the measurement of the SHWFS, to the extent that the measurement of a subaperture is biased as soon as the intensity distribution it receives is not uniform. The microlens array thus serves as a field sampler. That is why we investigate the effect of subapertures size on the robustness of the SHWFS measurement in the presence of scintillation in this paper.

For this purpose, we want to compare three SHWFS designs with different numbers of subapertures for a given telescope diameter of $D = 50\,\text{cm}$. For this study, we only use the MOSPAR9090 profile at elevation 10° and 30° (see Section 3). Given that the corresponding r_0 is between 2 and 4 cm, we first consider a reference design with 25x25 subapertures (SH25x25, $d_{subap} = 2\,\text{cm}$). Then, we consider an oversampled SHWFS with 50x50 subapertures (SH50x50, $d_{subap} = 1\,\text{cm}$) and an undersampled SHWFS with 10x10 subapertures (SH10x10, $d_{subap} = 5\,\text{cm}$). The study presented here is preliminary, in the sense that the measurement model does not take into account the noise or the range and saturation of the sensor yet. This simplification is made in order to isolate the measurement error induced by the discrepancy between Eq. 1 and Eq. 2 (see Section 2).

The measurement model is illustrated in Fig.2. The goal is to model the performance of the SHWFS when measuring a residual phase without modeling the whole AO system for now. From the simulated fields ψ obtained with PILOT, a field with a residual phase is calculated by correcting the field at a time t ($\psi(t)$) with $\frac{\psi(t-2)}{|\psi(t-2)|}$, the phase at time $t-2$. This corresponds to an ideal correction where an infinite number of modes have been sensed and corrected, with a two frame delay resulting in a residual wavefront φ_{in} due to temporal error only. Thus we obtain an operating point representative of a LEO link at 30° and 10°, without adding the error terms from the rest of the AO system, except temporal error. This field ψ_{in} is then used as the input of the SHWFS with or without the scintillation, i.e respectively with the amplitude variations of the field within the pupil or with a constant amplitude over the whole pupil. The slope measurement is performed by estimating the centroids of the PSFs using a classical Center of Gravity algorithm without thresholding: it is the Maximum Likelihood estimator in the case of a Gaussian PSF affected by photon noise only [6]. With and without scintillation, the SHWFS senses the field and then we reconstruct a phase φ_{rec} on a given set of Zernike modes. The more subapertures the SHWFS design has, the more modes we can reconstruct. For the SH50x50, we reconstruct 800 Zernike modes; for the SH25x25, 200 Zernike modes; and for the SH10x10, 65 Zernike modes. The reconstructed phase is then used as the correction phase. The final result of this model is the corrected field ψ_{corr}, resulting from the combination of the input amplitude A_{in} and the corrected phase $\varphi_{in} - \varphi_{rec}$.

Once the corrected field ψ_{corr} is obtained, a metric is needed to compare the performance of the three SHWFS designs. We consider the coupling efficiency of the corrected field into a SMF. It is an optical communication

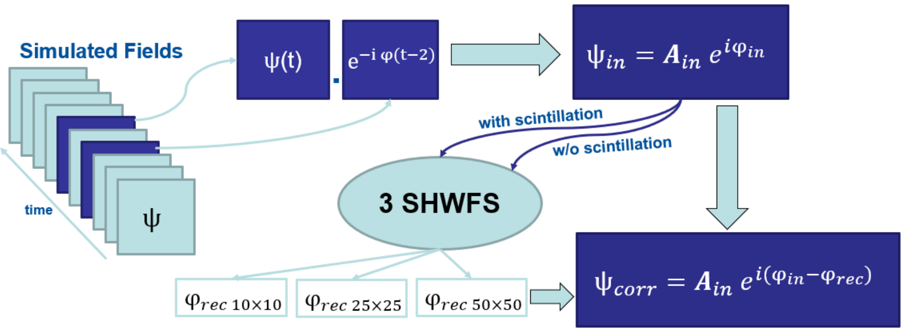

Figure 2: Model used in our simulations to estimate the impact of the scintillation on the performance of three configurations of SHWFS, without noise.

metric used to estimate the performance of an AO system. It is computed from the complex field, which avoids unwrapping the phase. At a given time t, its expression is given by:

$$\rho = \frac{\left|\int_{-\infty}^{+\infty} A_{in}(\mathbf{r}) e^{i(\varphi_{in}(\mathbf{r})-\varphi_{rec}(\mathbf{r}))} W_{SMF}(\mathbf{r}) P(\mathbf{r}) \mathrm{d}\mathbf{r}\right|^2}{\int_{-\infty}^{+\infty} |A_{in}(\mathbf{r})|^2 P(\mathbf{r}) \mathrm{d}\mathbf{r}} \tag{4}$$

where W_{SMF} is the normalized Gaussian mode of the SMF, and P is the aperture function of the telescope. We notice that the numerator involves the amplitude, and it is this weighing function that allows us to avoid the problem of branch points since $A_{in} = 0$ at these points. The denominator corresponds to a normalization by the Power in the Bucket (PIB) collected over the pupil. Thus, the coupling efficiency without phase or amplitude perturbation is 0.81 –the coupling of a plane wave with constant amplitude over the whole pupil with the Gaussian mode of the SMF, without occultation and $D/\omega_0 = 2.2$.

5. RESULTS AND DISCUSSION

Thanks to this measurement model, we obtain the coupling efficiency plots over time in the two scenarios of interest: in weak (Fig. 3) and in strong perturbation regimes (Fig. 4), respectively MOPSAR9090 at 30° and 10°.

The ideal coupling efficiency (without phase nor amplitude perturbation) $\rho_0 = 0.81$ is represented by a dashed black curve. This is the value reached in the case of a plane wavefront and a uniform intensity distribution across the pupil. The coupling efficiency with a perfect phase correction (solid black curve), or phase conjugation case, corresponds to the coupling of a plane wavefront with an amplitude perturbation only ($\psi_{corr} = A_{in}$). The variations of this curve are due to the fluctuation in the distribution of amplitude in the pupil. It is even possible that this curve exceeds the ideal rate in cases where the amplitude is distributed in such a way that it matches the Gaussian mode of the SMF better than a plane wave (some kind of lucky beam shaping). The colored curves correspond to the coupling efficiency with the phase correction corresponding to a phase reconstructed from the SHWFS data with and without scintillation, respectively the dashed and solid curves ($\psi_{corr} = A_{in} e^{i\varphi_{corr}}$). They follow the fluctuations of the phase conjugation case as can be expected since the amplitude is not corrected and it affects every case equally. Besides, they are shifted downwards as the quality of the correction decreases: with less reconstructed modes, the corrected wavefront is less flat and the coupling efficiency is lower.

In order to interpret the results, we can approximate the mean coupling efficiency as[12]:

$$\langle\rho\rangle \approx \rho_0\, e^{-\sigma_\chi^2}\, e^{-\sigma_{\varphi res}^2} \tag{5}$$

where σ_χ^2 is the log-amplitude variance, and $\sigma_{\varphi res}^2$ is the residual phase variance (after correction) computed over all occurrences.

In the phase conjugation case, $\sigma_\chi^2 \neq 0$ and $\sigma_{\varphi res}^2 = 0$. With weak perturbations, the mean value of the black solid curve is equal to the value of the approximation: $\langle\rho\rangle \approx e^{-\sigma_\chi^2} = 0.76$. But in the strong perturbation case,

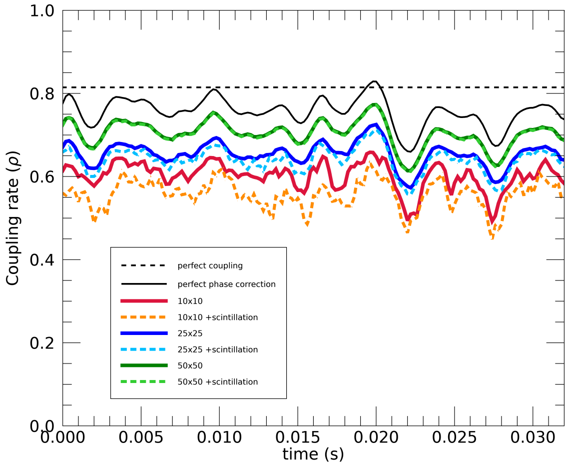

Figure 3: Coupled flux normalized by the PIB in the weak perturbation scenario (MOSPAR9090 profile at 30°). The dashed black line corresponds to the perfect coupling, and the solid black line corresponds to the phase conjugation case. The coloured lines corresponds to the cases of correction of the modes sensed by the 3 SHWFS configurations: with scintillation (dashed) and without (solid).

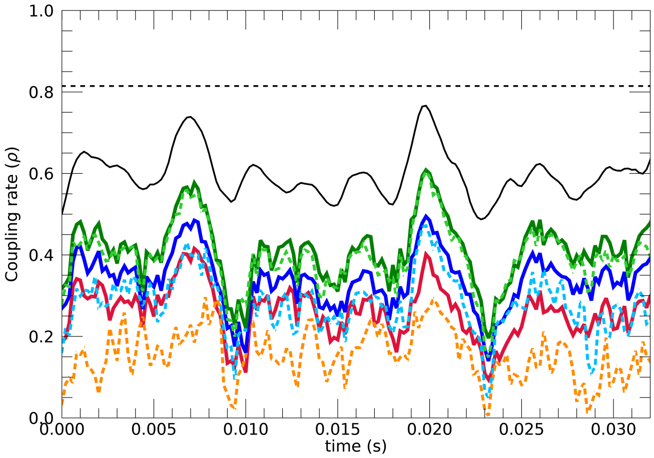

Figure 4: Coupled flux normalized by the PIB in the strong perturbations scenario (MOSPAR9090 profile at 10°). The dashed black line corresponds to the perfect coupling, and the solid black line corresponds to the phase conjugation case. The coloured lines corresponds to the cases of correction of the modes sensed by the 3 SHWFS configurations: with scintillation (dashed) and without (solid).

Eq. 5 gives $\langle\rho\rangle \approx 0.52$, whereas the mean value of the curve is 0.59. In fact, the approximation is less valid as the perturbations become stronger, but it still helps to understand the results qualitatively.

Then, regarding the solid colored curves, the downwards shift compared to the phase conjugation case can be explained by Eq. 5 as the residual phase error brought by the partial correction of the SHWFS: $\sigma^2_{\varphi res} = \sigma^2_{fitting} + \sigma^2_{aliasing}$, where $\sigma^2_{fitting}$ is the error due to the uncorrected Zernike modes, and $\sigma^2_{aliasing}$ is the error due to the finite sampling of the SHWFS. Since the SH50x50 measures more modes, it presents a lower error. Hence this design is the closest to the conjugated case, followed by the SH25x25 then the SH10x10.

When measurements are performed in the presence of scintillation, the residual phase error can be approximated as: $\sigma^2_{\varphi res} = \sigma^2_{fitting} + \sigma^2_{aliasing} + \sigma^2_{\varphi,scintillation}$. The latter corresponding to the measurement error induced by scintillation. Therefore, we can observe the impact of scintillation by comparing the solid and the dashed line of each SHWFS design, since the only difference is the presence of scintillation. In the low perturbation case given in Fig. 3, the effect of scintillation is quite small for the SH50x50 and SH25x25, but is a bit more noticeable for the SH10x10 case because the intensity distribution in these larger subapertures is significantly non uniform.

In the strong perturbation results given in Fig. 4, we see a clear difference between the performance of the 3 SHWFS designs. In this more scintillating case, we can really note the effect of scintillation on the SHWFS measurements. This effect is all the more important as the subapertures are large: scintillation patterns must be correctly sampled to avoid non-uniform intensity distribution. Indeed, the SH50x50 measurement is barely impacted by scintillation: the dashed curve and the solid curve are very close, while the performance of the SH10x10 decreases drastically in the presence of scintillation.

In these are preliminary results: we were able to point out the effect of the bias induced by the discrepancy between Eq. 1 and Eq. 2 on wavefront sensing. However in a real system, the noise and saturation level of the sensor – also related to scintillation – will lead to additional measurement errors that remain to be analysed.

Using all profiles presented in Section 3 and the corresponding simulated fields, we can study fluctuations of intensity between subapertures and inside subapertures. We want to highlight the difference between the three SHWFS designs regarding intensity distribution. The mean fluctuation of intensity between subapertures is computed as follows:

$$\frac{\langle \sigma^2_{I,between} \rangle_t}{\langle I_{subap}(t) \rangle^2_{grid,t}} = \frac{\langle \langle I^2_{subap}(t) \rangle_{grid} - \langle I_{subap}(t) \rangle^2_{grid} \rangle_t}{\langle I_{subap}(t) \rangle^2_{grid,t}} \tag{6}$$

where $I_{subap}(t)$ is the intensity integrated in the subapertures at each occurrence, and $\langle - \rangle_{grid}$ is an average over the subapertures grid. The mean fluctuation of intensity inside subapertures is computed as follows:

$$\frac{\langle \sigma^2_{I,inside} \rangle_t}{\langle I(t) \rangle^2_{pup,t}} = \frac{\langle \langle I^2(t) \rangle_{subap} - \langle I(t) \rangle^2_{subap} \rangle_{grid,t}}{\langle I(t) \rangle^2_{pup,t}} \tag{7}$$

where $I(t)$ is the intensity in the pixels, $\langle - \rangle_{subap}$ is an average over a subaperture, and $\langle - \rangle_{pup}$ is an average over the whole pupil. We show the evolution of these fluctuations as a function of $\sigma^2_{\chi Rytov}$ in Fig. 5. We observe that when the log-amplitude variance in Rytov regime increases, so does the fluctuations between and inside subapertures. Indeed, because of the relation between intensity and log-amplitude, $\sigma^2_{\chi Rytov}$ and the intensity variances are expected to follow the same trends, although the calculation supports differ. We also note that the intensity variations between subapertures of the SHWFS10x10 (in red) are lower than the ones of the two other SHWFS while its variations inside subapertures are higher. Thus, we have the expected effect of smaller subapertures: the intensity distribution is more uniform inside them. Nevertheless, with finer sampling of the pupil plane, the intensity is less uniformly distributed between subapertures resulting in a large dynamic range to

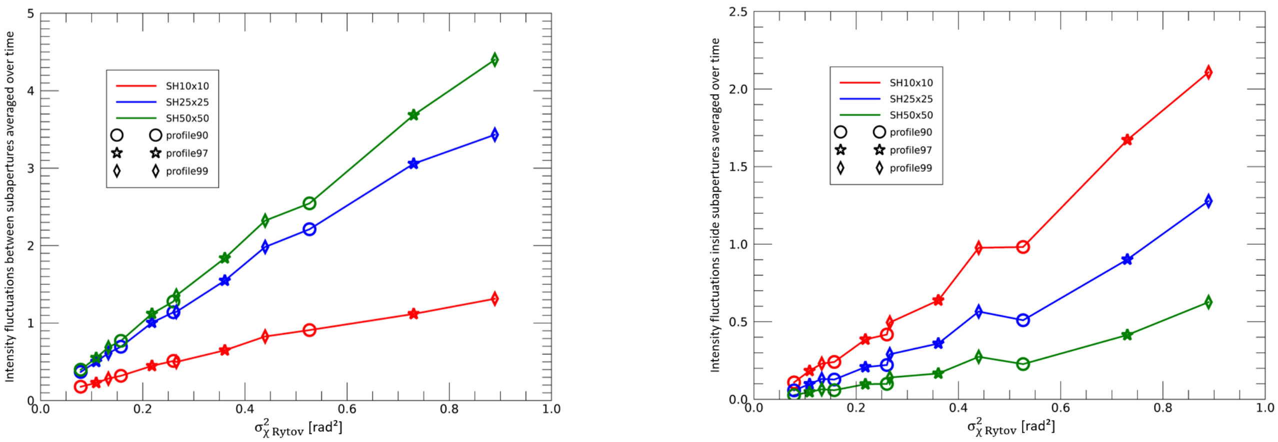

(a) Between subapertures

(b) Inside subapertures

Figure 5: Intensity fluctuations averaged over time versus log-amplitude variance computed using Rytov approximation. Each curve corresponds to a SHWFS design, and symbols indicate which profile each point is related to. (a) Mean intensity fluctuations between subapertures in the pupil. (b) Mean intensity fluctuations in the subapertures.

deal with, from extinguished subapertures to saturated ones. We will therefore have to use a detector with a large dynamic range, and a slope estimator efficient with every possible flux. The choice of the subapertures size is then a trade-off between reliability of measurements with scintillation, and complexity of reconstruction.

From the results presented in Fig. 3-4 and Fig. 5b, we can study the relation between the intensity distribution in the subapertures and its effect on the measurement error. Using Eq. 5, we consider that:

$$\sigma^2_{\varphi,scintillation} \approx -log(\frac{\langle\rho_{\ \ with\ \ \ scintillation}(t)\rangle_t}{\langle\rho_{\ \ without\ \ \ scintillation}(t)\rangle_t}) \qquad (8)$$

is the residual phase variance due to scintillation averaged over time. $\rho_{\ \ with\ \ \ scintillation}(t)$, and $\rho_{\ \ without\ \ \ scintillation}(t)$ respectively correspond to the coupling efficiency of the SHWFS configurations with and without scintillation (dashed and solid lines of Fig. 3-4). We can compute it from the output of the measurement model of Section 4 applied to all scenarios of Table 1. The result is shown in Fig. 6. Each curve stands for a specific turbulence profile at various elevations during the satellite pass in the sky.

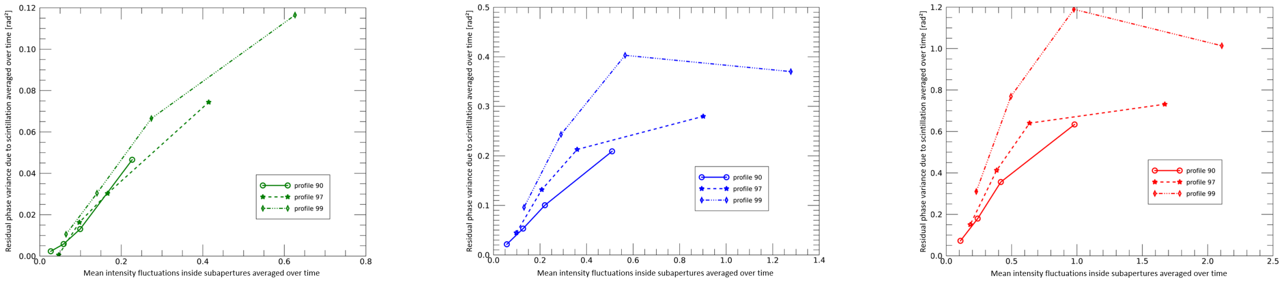

(a) SHWFS 50x50 (b) SHWFS 25x25 (c) SHWFS 10x10

Figure 6: Residual phase variance due to scintillation versus intensity fluctuations in the subapertures –both being averaged over time– for three SHWFS designs.

We observe that $\sigma^2_{\varphi,scintillation}$ increases with the fluctuations inside the subapertures. This further supports the fact that a more uniform intensity distribution induces a more accurate measurement. On top of that, for each profile, the curves seem to follow the same trends, with each SHWFS having its own slope. There seem to be a linear regime followed by a kind of saturation of $\sigma^2_{\varphi,scintillation}$ in the case of larger subapertures (i.e SHWFS25x25 and SHWFS50x50) with the most turbulent profile. This can be explained by the speckles getting smaller and independent. Then, thanks to aperture averaging[2], the error due to scintillation does not increase any further. It is not the case with the SHWFS50x50 because its subapertures are of comparable size with the scintillation pattern.

6. SUMMARY AND PERSPECTIVES

In this paper, we described a methodology to compare SHWFS designs in the presence of scintillation. We used the coupling efficiency metric to assess their performance and determine the optimal design for communication applications.

We focused on studying several sizes of subapertures, without noise nor sensor limitations, in two turbulence regimes representative of strong turbulence and scintillation conditions at 30° and 10° elevation. These preliminary results show that SHWFS with smaller subapertures are more robust to scintillation. Indeed, given that the SHWFS measures the phase gradient weighted by the intensity, a finer sampling of the pupil plane, closer to the size of the scintillation pattern, results in a more reliable measurement.

The next step is to account for noises and the dynamic range of the sensor to model more accurately the behavior of a SHWFS. The finite range of the sensor will imply some saturated subapertures, some missing measurements, and the detector and photon noises will affect the measurements accuracy. We will focus on studying slope measurement algorithms and determine the best suited one to face a large range of SNR induced by scintillation. We will then model a complete AO loop to globally optimize the system in strong perturbation regime with scintillation. Finally, an experimental implementation is planned on the PICOLO bench of ONERA to emulate the turbulence conditions of interest [11].

Acknowlegments

The authors wish to thank J. Osborn of Durham University for kindly providing Paranal's C_n^2 profiles database. This work was supported by DGA. This work was also supported by the Action Spécifique Haute Résolution Angulaire (ASHRA) of CNRS/INSU co-funded by CNES.

References

[1] Jeffrey D Barchers, David L Fried, and Donald J Link. "Evaluation of the performance of Hartmann sensors in strong scintillation". In: *Applied optics* 41.6 (2002), pp. 1012–1021.

[2] David L Fried. "Aperture averaging of scintillation". In: *JOSA* 57.2 (1967), pp. 169–175.

[3] ME Gracheva and AS Lezhen. "Fluctuations in the intensity of light propagated through a medium with varying turbulence". In: *Soviet Radiophysics* 9.1 (1966), pp. 37–39.

[4] Daniel Lechner et al. "Adaptable Shack-Hartmann wavefront sensor with diffractive lenslet arrays to mitigate the effects of scintillation". In: *Optics express* 28.24 (2020), pp. 36188–36205.

[5] Frederic Mahe et al. "Scintillation effects on wavefront sensing in the Rytov regime". In: *Propagation and Imaging through the Atmosphere IV*. Vol. 4125. SPIE. 2000, pp. 77–86.

[6] Magalie Nicolle et al. "Improvement of Shack–Hartmann wave-front sensor measurement for extreme adaptive optics". In: *Optics letters* 29.23 (2004), pp. 2743–2745.

[7] James Notaras and Carl Paterson. "Direct wavefront sensing for atmospheric adaptive optics in strong scintillation". In: *Advanced Wavefront Control: Methods, Devices, and Applications III*. Vol. 5894. SPIE. 2005, pp. 229–237.

[8] James Osborn et al. "Optical turbulence profiling with Stereo-SCIDAR for VLT and ELT". In: *Monthly Notices of the Royal Astronomical Society* 478.1 (2018), pp. 825–834.

[9] Charles A Primmerman et al. "Atmospheric-compensation experiments in strong-scintillation conditions". In: *Applied Optics* 34.12 (1995), pp. 2081–2088.

[10] Troy A Rhoadarmer. "Development of a self-referencing interferometer wavefront sensor". In: *Advanced Wavefront Control: Methods, Devices, and Applications II*. Vol. 5553. SPIE. 2004, pp. 112–126.

[11] Pablo Robles et al. "Emulating and characterizing strong turbulence conditions for space-to-ground optical links: The PICOLO bench". In: *JATIS* (2023, to be published).

[12] Cyril Ruilier and Frédéric Cassaing. "Coupling of large telescopes and single-mode waveguides: application to stellar interferometry". In: *JOSA A* 18.1 (2001), pp. 143–149.

[13] Nicolas Védrenne et al. "Performance analysis of an adaptive optics based optical feeder link ground station". In: *International Conference on Space Optics—ICSO 2020*. Vol. 11852. SPIE. 2021, pp. 527–535.